Observation of the Antimatter Hypernucleus ${}^{4}_{\bar{\Lambda}}\overline{\mathrm{H}}$

The STAR Collaboration∗

Matter-antimatter asymmetry is a research topic of fundamental interest, as it is the basis for the existence of the matter world, which survived annihilation with antimatter in the early Universe. High energy nuclear collisions create conditions similar to the Universe microseconds after the Big Bang, with comparable amounts of matter and antimatter. Much of the antimatter created escapes the rapidly expanding fireball without annihilation, making such collisions an effective experimental tool to create heavy antimatter nuclear objects and study their properties. In this paper, we report the first observation of the antimatter hypernucleus ${}^{4}_{\bar{\Lambda}}\overline{\mathrm{H}}$, composed of an $\bar{\Lambda}$, an antiproton and two antineutrons. The discovery was made through its two-body decay after production in ultrarelativistic heavy ion collisions by the STAR experiment at the Relativistic Heavy Ion Collider. In total, 15.6 candidate ${}^{4}_{\bar{\Lambda}}\overline{\mathrm{H}}$ antimatter hypernuclei are obtained with an estimated background count of 6.4. Lifetimes of the antihypernuclei ${}^{3}_{\bar{\Lambda}}\overline{\mathrm{H}}$ and ${}^{4}_{\bar{\Lambda}}\overline{\mathrm{H}}$ are measured and compared with lifetimes of their corresponding hypernuclei, testing the symmetry between matter and antimatter. Various production yield ratios among (anti)hypernuclei and (anti)nuclei are also measured and compared with theoretical model predictions, shedding light on their production mechanism.

In 1928, Paul Dirac found possible solutions with positive and negative energies to his eponymous equation that describes the relativistic quantum behavior of the electron [1]. It was realized in the following years that the negative energy solution actually indicates a new particle with the same mass as an electron, but the opposite charge [2]. This new particle was discovered by Carl Anderson

in cosmic rays in 1932 [3] and named the positron. This established the theoretical framework and the experimental foundation for the study of antimatter. With the advancement of detectors and accelerators, many more antimatter particles have been discovered. Figure 1 illustrates the masses vs. discovery years of a series of antimatter particles [3–11]. Among them, ${}^{4}_{\bar{\Lambda}}\overline{\mathrm{H}}$, whose discovery is described in this paper, is the heaviest antimatter nuclear and hypernuclear cluster observed to date.

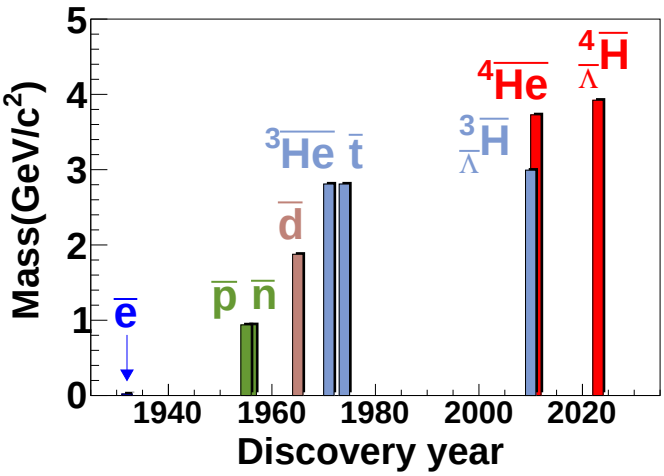

Figure 1: Masses of selected antimatter particles vs. their discovery years, focusing on the lineage of antimatter nuclear clusters.

Antimatter readily annihilates with matter, making it difficult to create antimatter nuclear clusters in the Universe. However relativistic heavy ion collisions can create the quark-gluon plasma state that existed in the first few microseconds of the Universe after the Big Bang, with nearly equal amounts of matter and antimatter [12–17]. The collision system expands and cools rapidly, allowing some antimatter to decouple from matter. This makes heavy ion collisions an effective tool to create and study antimatter nuclei [18–22].

A hyperon (e.g Λ) is a baryon containing at least one strange quark. A hypernucleus is a bound state of hyperons and nucleons. In this paper, the Solenoidal Tracker at RHIC (STAR) Collaboration [23] at the Relativistic Heavy Ion Collider (RHIC) reports the first observation of the antimatter hypernucleus ${}^{4}_{\bar{\Lambda}}\overline{\mathrm{H}}$, composed of an $\bar{\Lambda}$, an antiproton and two antineutrons. We also report the measurements of ${}^{3}_{\Lambda}\mathrm{H}$, ${}^{4}_{\Lambda}\mathrm{H}$, ${}^{3}_{\bar{\Lambda}}\overline{\mathrm{H}}$ and ${}^{4}_{\bar{\Lambda}}\overline{\mathrm{H}}$ lifetimes, and test matter-antimatter symmetry and CPT symmetry by hypernucleus-antihypernucleus lifetime comparisons. Various production yield ratios among (anti)hypernuclei and (anti)nuclei are measured and compared with theoretical model predictions, shedding light on the production mechanism of (anti)hypernuclei in relativistic heavy ion collisions.

(Anti)hypernucleus reconstruction

A total of about 6.4 billion U+U, Au+Au, Ru+Ru, and Zr+Zr collision events with center of mass energy per colliding nucleon-nucleon pair $\sqrt{s_{NN}}$=193 GeV (U+U) or 200 GeV (other systems) are used in this analysis. These data were collected in 2010, 2011, 2012 and 2018, with a variety of triggers, of which the minimum bias trigger recorded most of the events. The minimum bias trigger is designed to accept the events with different impact parameters as equally as possible.

(Anti)hypernuclei ${}^{3}_{\Lambda}\mathrm{H}$, ${}^{3}_{\bar{\Lambda}}\overline{\mathrm{H}}$, ${}^{4}_{\Lambda}\mathrm{H}$ and ${}^{4}_{\bar{\Lambda}}\overline{\mathrm{H}}$ are reconstructed through their two-body decay channels: ${}^{3}_{\Lambda}\mathrm{H}\rightarrow{}^{3}\mathrm{He}+\pi^{-}$, ${}^{3}_{\bar{\Lambda}}\overline{\mathrm{H}}\rightarrow{}^{3}\overline{\mathrm{He}}+\pi^{+}$, ${}^{4}_{\Lambda}\mathrm{H}\rightarrow{}^{4}\mathrm{He}+\pi^{-}$, and ${}^{4}_{\bar{\Lambda}}\overline{\mathrm{H}}\rightarrow{}^{4}\overline{\mathrm{He}}+\pi^{+}$. The charged daughter particles are detected and identified by the cylindrical Time Projection Chamber (TPC) [24] and Time of Flight detector (TOF) [25] placed inside the solenoidal magnetic field of 0.5 Tesla. The TPC re-

constructs the three-dimensional tracks and measures their rigidity (momentum over charge) and average ionization energy loss $\langle dE/dx \rangle$ in the gas. Figure 2(A) shows the measured $\langle dE/dx \rangle$ versus the rigidity of charged particles. Bands for different particle species can be seen in the figure. The curves show the expected trends for particles used in this analysis calculated with a Bichsel function [26]. The deviation of the measured $\langle dE/dx \rangle$ from the expected value for a certain particle species normalized by the resolution σ,

$$n_\sigma = \ln\left(\frac{\langle dE/dx \rangle}{\langle dE/dx \rangle_{\text{Bichsel}}}\right) / \sigma_{dE/dx}, \tag{1}$$

is defined and used for particle identification. The squared mass over charge (m^2/Z^2) of a particle is calculated from the rigidity, track length and time of flight measured by the TPC and TOF detectors. n_σ and m^2/Z^2 are used together for the selection of π^+, ^{3}He, ^{4}He and their corresponding antiparticles. Figures 2 (B) and (C) show $n_\sigma(^4\text{He})$ and $n_\sigma(^4\overline{\text{He}})$ versus the m^2/Z^2, for the selection of ^{4}He and $^4\overline{\text{He}}$ candidates.

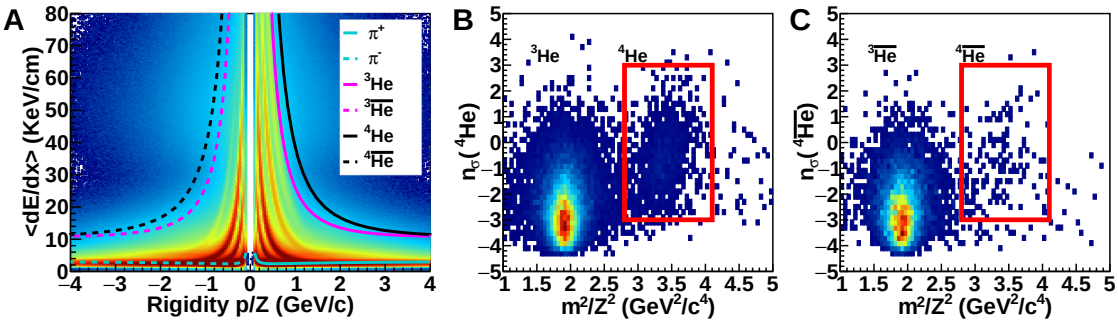

Figure 2: (A) $\langle dE/dx \rangle$ versus rigidity of charged particles measured by the TPC. The lines represent the Bichsel function calculations for π^+, ^{3}He and ^{4}He and their corresponding antiparticles. (B) and (C) show $n_\sigma(^4\text{He})$ and $n_\sigma(^4\overline{\text{He}})$ versus m^2/Z^2. The red boxes indicate the region for ^{4}He and $^4\overline{\text{He}}$ candidates.

(Anti)hypernucleus candidates are reconstructed from their decay daughters by the Kalman-Filter Particle Finder package [27,28]. In order to suppress background from random combinations of particles emitted from the collision point, selections have been applied such that the tracks of the two daughter particles are likely to come from a common decay vertex with significant displacement from the collision point. The selection cuts on the topological variables are optimized for the best ${}^{3}_{\Lambda}\overline{\mathrm{H}}$ signal, instead of ${}^{4}_{\Lambda}\overline{\mathrm{H}}$ signal, in order to avoid any bias towards a better signal and a larger yield of ${}^{4}_{\Lambda}\overline{\mathrm{H}}$ due to statistical fluctuations. This bias due to fluctuations is much smaller for ${}^{3}_{\Lambda}\overline{\mathrm{H}}$ because of its large signal significance.

Signals

The invariant mass spectra of reconstructed ${}^{3}_{\Lambda}\mathrm{H}$, ${}^{3}_{\Lambda}\overline{\mathrm{H}}$, ${}^{4}_{\Lambda}\mathrm{H}$, and ${}^{4}_{\Lambda}\overline{\mathrm{H}}$ candidates are shown in Fig. 3. Combinatorial backgrounds in the invariant mass distributions are reproduced with a rotation method, in which the (anti)helium nucleus track is randomly rotated by 30°-330° in azimuthal angle around the beam line before reconstructing the (anti)hypernucleus. In this way, the decay kinematics of the real signal candidate is destroyed and randomized as the combinatorial background. The rotation is done 50 times for each (anti)helium nucleus track in order to obtain a precise background shape, which is then normalized to match the two sides of the signal region. The final signal count is extracted by subtracting the combinatorial background from the signal distribution within the shaded invariant mass region in Fig. 3.

In total, 941 ± 59 ${}^{3}_{\Lambda}\mathrm{H}$, 637 ± 49 ${}^{3}_{\Lambda}\overline{\mathrm{H}}$, 24.4 ± 6.1 ${}^{4}_{\Lambda}\mathrm{H}$ and 15.6 ± 4.7 ${}^{4}_{\Lambda}\overline{\mathrm{H}}$ signal candidates are

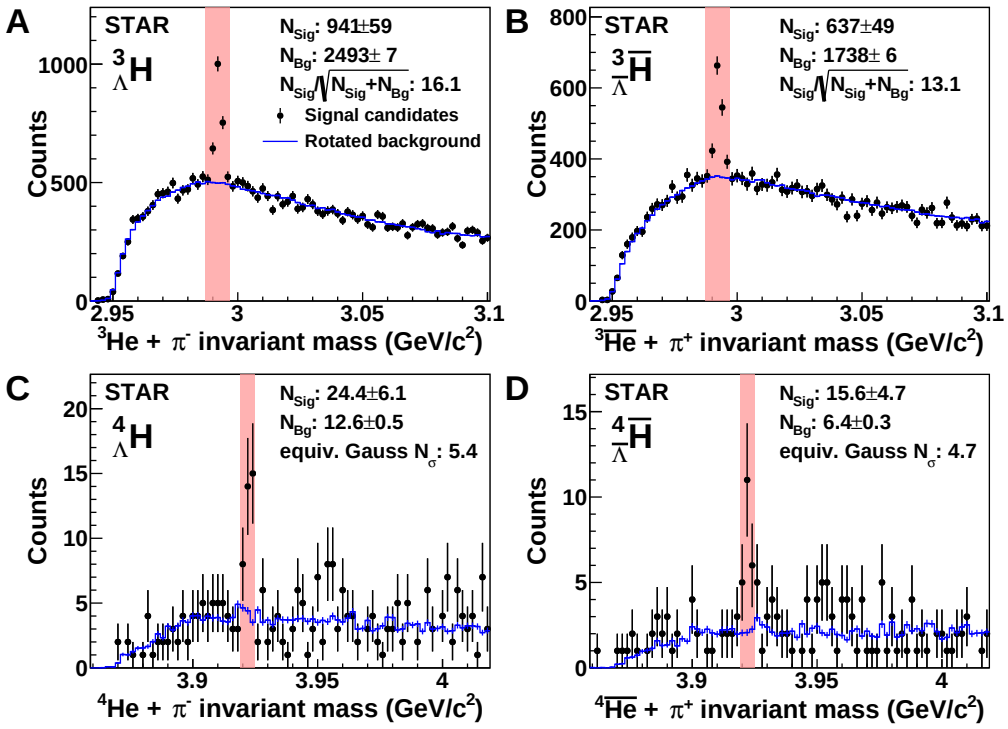

Figure 3: Invariant mass distributions of $^3\mathrm{He} + \pi^-$ (A), $^3\overline{\mathrm{He}} + \pi^+$ (B), $^4\mathrm{He} + \pi^-$ (C) and $^4\overline{\mathrm{He}} + \pi^+$ (D). The solid bands mark the signal invariant mass regions. The obtained signal count (N_{Sig}), background count (N_{Bg}), and signal significance are listed in each panel.

observed. The significances for $^3_\Lambda\mathrm{H}$, $^3_{\overline{\Lambda}}\overline{\mathrm{H}}$, $^4_\Lambda\mathrm{H}$, and $^4_{\overline{\Lambda}}\overline{\mathrm{H}}$ signals are 16.1, 13.1, 5.4, and 4.7 standard deviations, respectively. Here the $^3_\Lambda\mathrm{H}$ and $^3_{\overline{\Lambda}}\overline{\mathrm{H}}$ significances are calculated as $N_{\mathrm{Sig}}/\sqrt{N_{\mathrm{Sig}} + N_{\mathrm{Bg}}}$, where N_{Sig} is the signal count and N_{Bg} is the extracted background count. For $^4_\Lambda\mathrm{H}$ and $^4_{\overline{\Lambda}}\overline{\mathrm{H}}$, due to a very low background count, the proper distribution to describe the measured background is a Poisson distribution, rather than a Gaussian. Thus an equivalent Gaussian significance is introduced, in order to describe the possibility that the background with an expected value of N_{Bg} fluctuates to the measured total candidate count $N_{\mathrm{Sig}} + N_{\mathrm{Bg}}$.

Lifetimes and matter-antimatter symmetry test

Our current knowledge of physics principles suggests that the early Universe should have contained equal amounts of matter and antimatter. However, the antiproton flux in cosmic rays and other measurements [29] indicate that no large-scale antimatter exists in the vicinity of our galaxy, and the visible universe is almost entirely matter. Naturally, one may ask where the antimatter is, and what causes this matter-antimatter asymmetry in the Universe? According to the CPT theorem, physical laws should remain unchanged under the combined operation of CPT, where C is charge conjugation, P is parity transformation and T is time reversal [30]. Comparing the properties like mass and lifetime of a particle and its corresponding antiparticle is an important experimental way to test the CPT symmetry [31] and to search for new mechanisms that cause matter and antimatter asymmetry in the Universe. Recently, the ALICE and STAR experiments reported that there is no significant mass (binding energy) difference between deuteron and antideuteron [22], between ^{3}He and $^3\overline{\text{He}}$ [22] and between ${}^3_\Lambda$H and ${}^3_{\overline{\Lambda}}\overline{\text{H}}$ [19]. ALICE has also measured the relative difference between ${}^3_\Lambda$H and ${}^3_{\overline{\Lambda}}\overline{\text{H}}$ lifetimes, which is consistent with zero [32].

Hypernuclei lifetimes are also a good probe to study the interaction between hyperons and nucleons in it, which is important for understanding the inner structure of compact stellar objects like neutron stars [33]. Numerous measurements of the lifetimes of hypernuclei [20,34–43] show slightly shorter average lifetimes of ${}^3_\Lambda$H and ${}^4_\Lambda$H than that of the Λ hyperon. The combined lifetimes of ${}^3_\Lambda$H and ${}^3_{\overline{\Lambda}}\overline{\text{H}}$ have also been measured [10,32,41,44].

In this study, the lifetimes of (anti)hypernuclei ${}^3_\Lambda$H, ${}^4_\Lambda$H, ${}^3_{\overline{\Lambda}}\overline{\text{H}}$ and ${}^4_{\overline{\Lambda}}\overline{\text{H}}$ are measured. In order to

avoid the low transverse momentum (p_T) region, where the reconstruction efficiency approaches zero and may have relatively large systematic uncertainties, the measurement is performed only for (anti)hypernuclei with $p_T > 2.1$ GeV/c. (Anti)hypernucleus signal yields in $ct = L/\beta\gamma = L/(p/m)$ intervals are obtained as described in the section above, where c, t, L, β, γ, p and m represent the speed of light, the decay time, the measured decay length, the ratio of velocity to c, the Lorentz factor, the measured momentum and the (anti)hypernucleus nominal mass, respectively. The reconstruction efficiencies of ${}^{3}_{\Lambda}\mathrm{H}$, ${}^{3}_{\bar{\Lambda}}\overline{\mathrm{H}}$, ${}^{4}_{\Lambda}\mathrm{H}$ and ${}^{4}_{\bar{\Lambda}}\overline{\mathrm{H}}$ in each $L/\beta\gamma$ bin are evaluated by a Monte Carlo method in which (anti)hypernuclei are simulated using the GEANT3 [45] software package and embedded in real collision events. In this way, the simulated (anti)hypernuclei are reconstructed in a realistic environment. Efficiency-corrected yields of ${}^{3}_{\Lambda}\mathrm{H}$, ${}^{3}_{\bar{\Lambda}}\overline{\mathrm{H}}$, ${}^{4}_{\Lambda}\mathrm{H}$ and ${}^{4}_{\bar{\Lambda}}\overline{\mathrm{H}}$ as a function of $L/\beta\gamma$ are shown in Fig.4(A). The lifetimes τ are extracted by fitting the data with the expression $N(t) = N_0 \exp(-t/\tau) = N_0 \exp(-(L/\beta\gamma)/c\tau)$. Variations of parameters used in the signal reconstruction and efficiency calculation are applied to obtain the systematic uncertainties of the measured lifetimes.

The extracted ${}^{3}_{\Lambda}\mathrm{H}$, ${}^{3}_{\bar{\Lambda}}\overline{\mathrm{H}}$, ${}^{4}_{\Lambda}\mathrm{H}$ and ${}^{4}_{\bar{\Lambda}}\overline{\mathrm{H}}$ lifetimes are shown in Fig. 4(B). Within uncertainties, our results are consistent with existing measurements[10,20,32,34–44] and theory predictions [46–51]. The lifetime differences between hypernuclei and their corresponding antihypernuclei are $\tau_{{}^{3}_{\Lambda}\mathrm{H}} - \tau_{{}^{3}_{\bar{\Lambda}}\overline{\mathrm{H}}}$ =16 $\pm$ 43(stat.) $\pm$ 20(sys.) ps and $\tau_{{}^{4}_{\Lambda}\mathrm{H}} - \tau_{{}^{4}_{\bar{\Lambda}}\overline{\mathrm{H}}}$ =18 $\pm$ 115(stat.) $\pm$ 46(sys.) ps. Both are consistent with zero within uncertainties. This is a new test of the matter-antimatter and CPT symmetry.

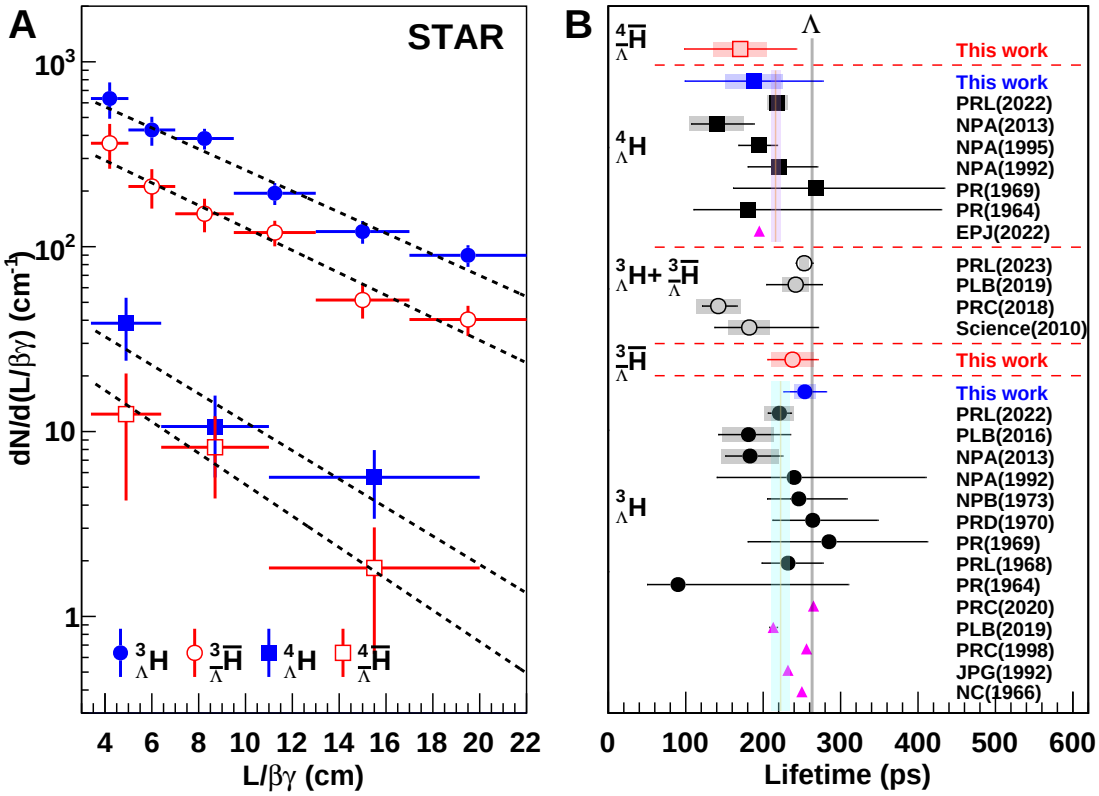

Figure 4: (A) ${}^{3}_{\Lambda}\mathrm{H}$, ${}^{3}_{\bar{\Lambda}}\overline{\mathrm{H}}$, ${}^{4}_{\Lambda}\mathrm{H}$ and ${}^{4}_{\bar{\Lambda}}\overline{\mathrm{H}}$ yields versus $L/\beta\gamma$. The vertical error bars represent the statistical error only. (B) Our measured ${}^{3}_{\Lambda}\mathrm{H}$, ${}^{3}_{\bar{\Lambda}}\overline{\mathrm{H}}$, ${}^{4}_{\Lambda}\mathrm{H}$ and ${}^{4}_{\bar{\Lambda}}\overline{\mathrm{H}}$ lifetimes compared with world data [10,20,32,34–44] and theoretical predictions [46–51] (solid triangles). Error bars and boxes represent statistical and systematic uncertainties, respectively. Vertical solid lines with shaded regions show the average lifetime of ${}^{3}_{\Lambda}\mathrm{H}$ and ${}^{4}_{\Lambda}\mathrm{H}$ and their corresponding uncertainties. The vertical gray line shows the lifetime of the free Λ.

Yield ratios

The (anti)nucleus and (anti)hypernucleus production yields are sensitive to the evolution of the fireball, the strange baryon freeze-out dynamics, and the (anti)hypernucleus production mechanism in relativistic heavy ion collisions[52]. The statistical thermal model [53] works reasonably well in describing particle production yields including (anti)nuclei and (anti)hypernuclei. In this model, all particles are assumed to be in a thermal and chemical equilibrium, and the chemical freeze-out temperature T and baryon chemical potential μ_B parameters can be obtained by a simultaneous fit to all existing measured particle yields. For heavy ion collisions at an energy around 200 GeV per nucleon-nucleon pair, the chemical freeze-out temperature is around 164 MeV [53]. Thus the (anti)nuclei and (anti)hypernuclei in the collision system, with typical binding energies of merely several MeV per (anti)baryon, are like snowballs in an oven. A commonly accepted microscopic explanation for this contradiction is that (anti)nuclei and (anti)hypernuclei are produced at the last stage of the collision system evolution, via coalescence of (anti)hyperons and (anti)nucleons that are close in both coordinate and momentum space[54,55]. This coalescence mechanism can successfully describe the existing (anti)nuclei and (anti)hypernucleus production yield and yield ratio measurements [10,11,20,21,56] after taking into account their baryon number, strangeness number and spin degeneracy. Knowledge of (anti)hypernucleus production can also help us to estimate the possibility of producing and observing more exotic entities, such as strangelets[57,58] and strange hadronic matter[59], in relativistic heavy ion collisions.

In this analysis we use a combination of data from U+U, Au+Au, Ru+Ru, and Zr+Zr colli-

sions. Absolute particle production yields are different in different collision systems. We therefore measure various yield ratios between particles with the same baryon number instead of absolute yields of each particle, so that the effect due to different collision system sizes will largely cancel out. We conduct the yield ratio measurements with only minimum bias triggered events, in order to avoid possible bias by trigger selection. The measurement is done with particles in a phase space region of rapidity $|y| < 0.7$ and $0.7c < p_T/m < 1.5c$. Acceptance and efficiency are corrected for using the above-mentioned Monte Carlo simulation. The branching fractions of the (anti)hypernuclei two-body decay channels used in this analysis, 0.25 for ${}^{3}_{\Lambda}\mathrm{H}$ and ${}^{3}_{\Lambda}\overline{\mathrm{H}}$ and 0.5 for ${}^{4}_{\Lambda}\mathrm{H}$ and ${}^{4}_{\Lambda}\overline{\mathrm{H}}$ following previous measurements[42], are also corrected for. ${}^{3}\mathrm{He}$, ${}^{3}\overline{\mathrm{He}}$, ${}^{4}\mathrm{He}$, and ${}^{4}\overline{\mathrm{He}}$ yields are corrected for contributions from ${}^{3}_{\Lambda}\mathrm{H}$, ${}^{3}_{\Lambda}\overline{\mathrm{H}}$, ${}^{4}_{\Lambda}\mathrm{H}$, and ${}^{4}_{\Lambda}\overline{\mathrm{H}}$ decays when calculating the ratios. The systematic uncertainties of the yield ratios are estimated by varying the signal reconstruction, yield extraction and efficiency correction procedures.

Figure 5 shows the measured particle production yield ratios and a comparison to previous experimental results[10,11,20,60], as well as the thermal model predictions[53]. The ${}^{3}\overline{\mathrm{He}}/{}^{3}\mathrm{He}$, ${}^{4}\overline{\mathrm{He}}/{}^{4}\mathrm{He}$ and ${}^{3}_{\Lambda}\overline{\mathrm{H}}/{}^{3}_{\Lambda}\mathrm{H}$ ratios are in good agreement with the previous STAR measurements [10,11]. For the ${}^{3}_{\Lambda}\mathrm{H}/{}^{3}\mathrm{He}$ and ${}^{3}_{\Lambda}\overline{\mathrm{H}}/{}^{3}\overline{\mathrm{He}}$ ratios, since some collision system size dependence is expected [61], we have also conducted the measurement in large (U+U, Au+Au) and small (Zr+Zr, Ru+Ru) systems separately, in order to compare with existing measurements. The measured ${}^{3}_{\Lambda}\mathrm{H}/{}^{3}\mathrm{He}$ and ${}^{3}_{\Lambda}\overline{\mathrm{H}}/{}^{3}\overline{\mathrm{He}}$ ratios in U+U and Au+Au collisions are lower than previous STAR results [10] by 2.8 and 1.9 σ, respectively.

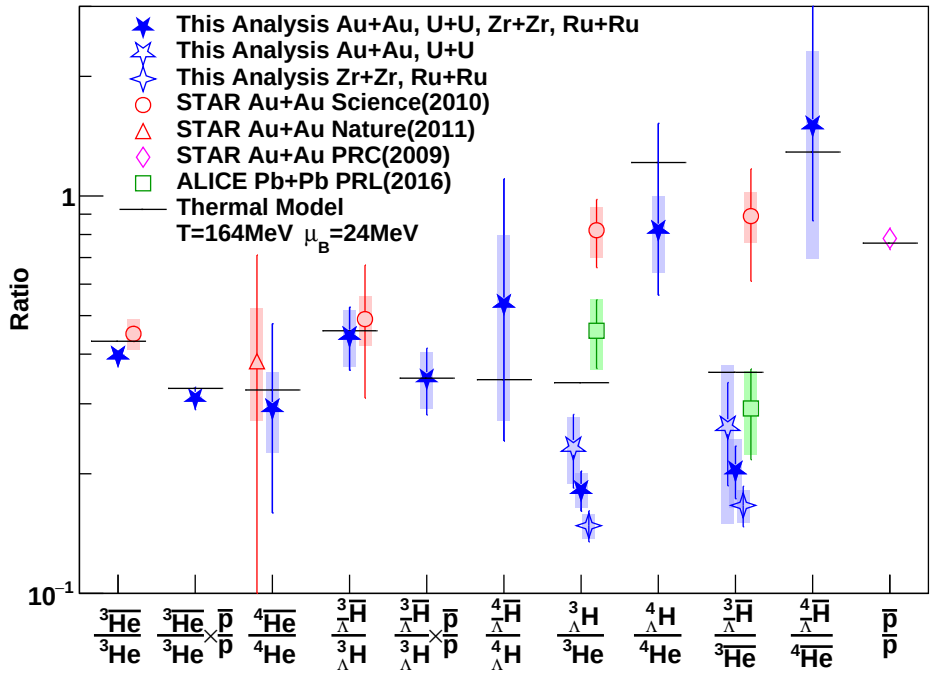

Figure 5: Production yield ratios of various particles with the same baryon number. Results combining all collision systems in this work are shown by filled stars. Open stars show results with only U+U and Au+Au collisions, while quadrangular stars show results with only Zr+Zr and Ru+Ru collisions. Statistical uncertainties and systematic uncertainties are shown by vertical bars and boxes, respectively. Previous measurement results[10,11,20,60] and thermal model predictions[53] are also shown for comparison.

Various antimatter-over-matter particle yield ratios are measured to be below unity because the colliding heavy ions carry positive baryon numbers, and consequently the collision system has positive baryon chemical potential. The measured $^4\overline{\mathrm{He}}/^4\mathrm{He}$ and ${}^4_{\bar{\Lambda}}\overline{\mathrm{H}}/{}^4_{\Lambda}\mathrm{H}$ ratios are consistent with the combined ratios of $^3\overline{\mathrm{He}}/^3\mathrm{He} \times \bar{\mathrm{p}}/\mathrm{p}$ and ${}^3_{\bar{\Lambda}}\overline{\mathrm{H}}/{}^3_{\Lambda}\mathrm{H} \times \bar{\mathrm{p}}/\mathrm{p}$, respectively. This is expected in the coalescence [54,55] and thermal [53] models of (anti)nucleus and (anti)hypernucleus production, as the total baryon number, strangeness and spin degeneracy are the same for the corresponding numerators and denominators of the two ratios [42,62].

In the (anti)hypernucleus over (anti)nucleus ratios, ${}^3_{\Lambda}\mathrm{H}/^3\mathrm{He}$, ${}^3_{\bar{\Lambda}}\overline{\mathrm{H}}/^3\overline{\mathrm{He}}$, ${}^4_{\Lambda}\mathrm{H}/^4\mathrm{He}$ and ${}^4_{\bar{\Lambda}}\overline{\mathrm{H}}/^4\overline{\mathrm{He}}$, the baryon number effect cancels out between the numerators and denominators, and the strangeness number effect is the same for ${}^3_{\Lambda}\mathrm{H}/^3\mathrm{He}$ vs ${}^4_{\Lambda}\mathrm{H}/^4\mathrm{He}$, and for ${}^3_{\bar{\Lambda}}\overline{\mathrm{H}}/^3\overline{\mathrm{He}}$ vs ${}^4_{\bar{\Lambda}}\overline{\mathrm{H}}/^4\overline{\mathrm{He}}$. The spin degeneracy effect also cancels out for ${}^3_{\Lambda}\mathrm{H}/^3\mathrm{He}$ and ${}^3_{\bar{\Lambda}}\overline{\mathrm{H}}/^3\overline{\mathrm{He}}$, since all these $A = \pm 3$ (anti)nuclei and (anti)hypernuclei have spin of 1/2. However, unlike other (hyper)nuclei considered here, both spin 0 and spin 1 states of ${}^4_{\Lambda}\mathrm{H}$ have enough binding energy so that no energetically allowed strong decay channels exist for them. So the spin 1 state, with a spin degeneracy of 3, will decay electromagnetically to the spin 0 ground state. This enhances the total measured ${}^4_{\Lambda}\mathrm{H}$ and ${}^4_{\bar{\Lambda}}\overline{\mathrm{H}}$ production yield by a factor of 4, compared to $^4\mathrm{He}$ and $^4\overline{\mathrm{He}}$ which have only a spin 0 state [42]. Thus according to the coalescence model, ${}^4_{\Lambda}\mathrm{H}/^4\mathrm{He}$ and ${}^4_{\bar{\Lambda}}\overline{\mathrm{H}}/^4\overline{\mathrm{He}}$ are expected to be about 4 times higher than ${}^3_{\Lambda}\mathrm{H}/^3\mathrm{He}$ and ${}^3_{\bar{\Lambda}}\overline{\mathrm{H}}/^3\overline{\mathrm{He}}$, respectively. This agrees well with our measurements shown in Fig. 5.

All the measured particle production yield ratios are also compared with predictions from the statistical thermal model [53]. Considering the ${}^4_{\Lambda}\mathrm{H}$ and ${}^4_{\bar{\Lambda}}\overline{\mathrm{H}}$ spin degeneracy effects mentioned

above, the thermal model predictions also match our measurements well in Fig. 5, except that the measured ${}^{3}_{\Lambda}\mathrm{H}/{}^{3}\mathrm{He}$ ratio is slightly lower than the thermal model prediction. This difference, if really exists, may be explained by the smaller binding energy and larger size of ${}^{3}_{\Lambda}\mathrm{H}$ than ${}^{3}\mathrm{He}$ [56].

According to the coalescence model and statistical thermal model, antinucleus and antihypernucleus production yields decrease by about 3 orders of magnitude for each additional atomic mass number [11,53]. Thirteen years after the discovery of the first antihypernucleus ${}^{3}_{\bar{\Lambda}}\overline{\mathrm{H}}$, the discovery of ${}^{4}_{\bar{\Lambda}}\overline{\mathrm{H}}$ and the related matter-antimatter symmetry test as well as yield ratio measurements are a great step forward in the experimental research of antimatter.

Acknowledgement

We thank the RHIC Operations Group and RCF at BNL, the NERSC Center at LBNL, and the Open Science Grid consortium for providing resources and support. This work was supported in part by the Office of Nuclear Physics within the U.S. DOE Office of Science, the U.S. National Science Foundation, National Natural Science Foundation of China, Chinese Academy of Science, the Ministry of Science and Technology of China and the Chinese Ministry of Education, the Higher Education Sprout Project by Ministry of Education at NCKU, the National Research Foundation of Korea, Czech Science Foundation and Ministry of Education, Youth and Sports of the Czech Republic, Hungarian National Research, Development and Innovation Office, New National Excellency Programme of the Hungarian Ministry of Human Capacities, Department of Atomic Energy and Department of Science and Technology of the Government of India, the Na-

tional Science Centre and WUT ID-UB of Poland, the Ministry of Science, Education and Sports of the Republic of Croatia, German Bundesministerium für Bildung, Wissenschaft, Forschung and Technologie (BMBF), Helmholtz Association, Ministry of Education, Culture, Sports, Science, and Technology (MEXT) and Japan Society for the Promotion of Science (JSPS).

Reference

1. Dirac, P. A. The Quantum Theory of the Electron. *Proc. Roy. Soc. Lond. A* **117**, 610–624 (1928).

2. Dirac, P. A. Quantised Singularities in the Electromagnetic Field. *Proc. Roy. Soc. Lond. A* **133**, 60–72 (1931).

3. Anderson, C. The Positive Electron. *Phys. Rev.* **43**, 491–494 (1933).

4. Chamberlain, O., Segre, E., Wiegand, C. & Ypsilantis, T. Observation of Anti-Protons. *Phys. Rev.* **100**, 947–950 (1955).

5. Cork, B., Lambertson, G. R., Piccioni, O. & Wenzel, W. A. Anti-neutrons Produced from Anti-protons in Charge Exchange Collisions. *Phys. Rev.* **104**, 1193–1197 (1957).

6. Massam, T., Muller, T., Righini, B., Schneegans, M. & Zichichi, A. Experimental Observation of Antideuteron Production. *Nuovo Cim.* **39**, 10–14 (1965).

7. Dorfan, D. E., Eades, J., Lederman, L. M., Lee, W. & Ting, C. C. Observation of Antideuterons. *Phys. Rev. Lett.* **14**, 1003–1006 (1965).

8. Antipov, Y. M. *et al.* Observation of Anti-he-3. *Yad. Fiz.* **12**, 311–322 (1970).

9. Vishnevsky, N. K. *et al.* Observation of Anti-Tritium. *Yad. Fiz.* **20**, 694–708 (1974).

10. Abelev, B. I. *et al.* Observation of an Antimatter Hypernucleus. *Science* **328**, 58–62 (2010). 1003.2030.

11. Agakishiev, H. *et al.* Observation of the Antimatter Helium-4 Nucleus. *Nature* **473**, 353 (2011). [Erratum: Nature 475, 412 (2011)], 1103.3312.

12. Adams, J. *et al.* Experimental and Theoretical Challenges in the Search for the Quark Gluon Plasma: The STAR Collaboration's Critical Assessment of the Evidence from RHIC Collisions. *Nucl. Phys. A* **757**, 102–183 (2005). nucl-ex/0501009.

13. Adcox, K. *et al.* Formation of Dense Partonic Matter in Relativistic Nucleus-Nucleus Collisions at RHIC: Experimental Evaluation by the PHENIX Collaboration. *Nucl. Phys. A* **757**, 184–283 (2005). nucl-ex/0410003.

14. Back, B. B. *et al.* The PHOBOS Perspective on Discoveries at RHIC. *Nucl. Phys. A* **757**, 28–101 (2005). nucl-ex/0410022.

15. Arsene, I. *et al.* Quark Gluon Plasma and Color Glass Condensate at RHIC: The Perspective from the BRAHMS Experiment. *Nucl. Phys. A* **757**, 1–27 (2005). nucl-ex/0410020.

16. Muller, B., Schukraft, J. & Wyslouch, B. First Results from Pb+Pb Collisions at the LHC. *Ann. Rev. Nucl. Part. Sci.* **62**, 361–386 (2012). 1202.3233.

17. Adam, J. *et al.* Beam energy dependence of (anti-)deuteron production in Au + Au collisions at the BNL Relativistic Heavy Ion Collider. *Phys. Rev. C* **99**, 064905 (2019). 1903.11778.

18. Chen, J., Keane, D., Ma, Y.-G., Tang, A. & Xu, Z. Antinuclei in Heavy-Ion Collisions. *Phys. Rept.* **760**, 1–39 (2018). 1808.09619.

19. Adam, J. *et al.* Measurement of the Mass Difference and the Binding Energy of the Hypertriton and Antihypertriton. *Nature Phys.* **16**, 409–412 (2020). 1904.10520.

20. Adam, J. *et al.* ${}^{3}_{\Lambda}\mathrm{H}$ and ${}^{3}_{\Lambda}\overline{\mathrm{H}}$ Production in Pb-Pb Collisions at $\sqrt{s_{\mathrm{NN}}} = 2.76$ TeV. *Phys. Lett. B* **754**, 360–372 (2016). 1506.08453.

21. Acharya, S. *et al.* Production of ^{4}He and ${}^{4}\overline{\mathrm{He}}$ in Pb-Pb Collisions at $\sqrt{s_{\mathrm{NN}}}$ = 2.76 TeV at the LHC. *Nucl. Phys. A* **971**, 1–20 (2018). 1710.07531.

22. Adam, J. *et al.* Precision Measurement of the Mass Difference between Light Nuclei and Anti-nuclei. *Nature Phys.* **11**, 811–814 (2015). 1508.03986.

23. Ackermann, K. *et al.* STAR Detector Overview. *Nuclear Instruments and Methods A* **499**, 624–632 (2003).

24. Anderson, M. *et al.* The STAR Time Projection Chamber: a Unique Tool for Studying High Multiplicity Events at RHIC. *Nuclear Instruments and Methods A* **499**, 659–678 (2003).

25. Llope, W. J. and STAR collaboration et al. Multigap RPCs in the STAR Experiment at RHIC. *Nuclear Instruments and Methods A* **661**, S110–S113 (2012).

26. Bichsel, H. A Method to Improve Tracking and Particle Identification in TPCs and Silicon Detectors. *Nuclear Instruments and Methods A* **562**, 154–197 (2006).

27. Kisel, I., Kulakov, I. & Zyzak, M. Standalone First Level Event Selection Package for the CBM Experiment. In *Proceedings, 18th Real-Time Conference (RT2012) : Berkley, USA, June 11-15, 2012* (2012).

28. Zyzak, M. *Online Selection of Short-lived Particles on Many-core Computer Architectures in the CBM Experiment at FAIR*. Ph.D. thesis, Johann Wolfgang Goethe-Universität (2016).

29. Aguilar, M. *et al.* Antiproton Flux, Antiproton-to-Proton Flux Ratio, and Properties of Elementary Particle Fluxes in Primary Cosmic Rays Measured with the Alpha Magnetic Spectrometer on the International Space Station. *Phys. Rev. Lett.* **117**, 091103 (2016).

30. Luders, G. On the Equivalence of Invariance under Time Reversal and under Particle-Antiparticle Conjugation for Relativistic Field Theories. *Kong. Dan. Vid. Sel. Mat. Fys. Med.* **28N5**, 1–17 (1954).

31. Group, P. D. *et al.* Review of Particle Physics. *Progress of Theoretical and Experimental Physics* **2022**, 083C01 (2022).

32. Acharya, S. *et al.* Measurement of the Lifetime and Λ Separation Energy of HΛ3. *Phys. Rev. Lett.* **131**, 102302 (2023). 2209.07360.

33. Gal, A., Hungerford, E. V. & Millener, D. J. Strangeness in Nuclear Physics. *Rev. Mod. Phys.* **88**, 035004 (2016).

34. Prem, R. J. *et al.* Lifetimes of Hypernuclei, ${}^{3}_{\Lambda}\mathrm{H}$, ${}^{4}_{\Lambda}\mathrm{H}$, ${}^{5}_{\Lambda}\mathrm{H}$. *Phys. Rev.* **136**, B1803 (1964).

35. Keyes, G. *et al.* New Measurement of the ${}^{3}_{\Lambda}H$. *Phys. Rev. Lett.* **20**, 819–821 (1968).

36. Phillips, R. E. *et al.* Lifetimes of Light Hyperfragments. II. *Phys. Rev.* **180**, 1307 (1964).

37. Keys, G. *et al.* Properties of ${}^{3}_{\Lambda}H$. *Phys. Rev. D* **1**, 66–77 (1970).

38. Keys, G. *et al.* A Measurement of the Lifetime of the ${}^{3}_{\Lambda}\mathrm{H}$ Hypernucleus. *Nucl. Phys. B* **67**, 269–283 (1973).

39. Avramenko, S. *et al.* A Study of the Production and Lifetime of the Lightest Relativistic Hypernuclei. *Nucl. Phys. A* **547**, 95c (1992).

40. Rappold, C. *et al.* Hypernuclear Spectroscopy of Products from ^{6}Li Projectiles on a Carbon Target at 2 A GeV. *Nucl. Phys. A* **913**, 170–184 (2013).

41. Adamczyk, L. *et al.* Measurement of the ${}^{3}_{\Lambda}\mathrm{H}$ lifetime in Au+Au collisions at the BNL Relativistic Heavy Ion Collider. *Phys. Rev. C* **97**, 054909 (2018). 1710.00436.

42. Abdallah, M. *et al.* Measurements of H^{3}_{Λ} and H^{4}_{Λ} Lifetimes and Yields in Au+Au Collisions in the High Baryon Density Region. *Phys. Rev. Lett.* **128**, 202301 (2022). 2110.09513.

43. Outa, H. *et al.* Mesonic Weak Decay of ${}^{4}_{\Lambda}H$ and ${}^{4}_{\Lambda}He$. *Nucl. Phys. A* **585**, 109c (1995).

44. Acharya, S. *et al.* ${}^{3}_{\Lambda}\mathrm{H}$ and ${}^{3}_{\Lambda}\overline{\mathrm{H}}$ lifetime measurement in Pb-Pb collisions at $\sqrt{s_{\mathrm{NN}}} = 5.02$ TeV via two-body decay. *Phys. Lett. B* **797**, 134905 (2019). 1907.06906.

45. Brun, R., Bruyant, F., Maire, M., McPherson, A. C. & Zanarini, P. GEANT3 (1987).

46. Rayet, M. *et al.* The Lifetime of ${}^{3}_{\Lambda}$H. *Nuovo Cimento* **XLVI**, 8302–8310 (1966).

47. Congleton, J. G. A Simple Model of the Hypertriton. *J. Phys. G: Nucl. Part. Phys.* **18**, 339–357 (1992).

48. Kamada, H. *et al.* π-mesonic Decay of the Hypertriton. *Phys. Rev. C* **57**, 1595–1603 (1998).

49. Gal, A. *et al.* Towards Resolving the ${}^{3}_{\Lambda}$H Lifetime Puzzle. *Phys. Lett. B* **791**, 48–53 (2019).

50. Hidenbrand, F. *et al.* Lifetime of the Hypertriton. *Phys. Rev. C* **102**, 064002 (2020).

51. Gal, A. Recent Progress on few-body Hypernuclei. *EPJ Web Conf.* **259**, 08002 (2022).

52. Sun, K.-J. & Chen, L.-W. Antimatter ${}^{4}_{\Lambda}\mathrm{H}$ Hypernucleus Production and the ${}^{3}_{\Lambda}\mathrm{H}/{}^{3}\mathrm{He}$ Puzzle in Relativistic Heavy-Ion Collisions. *Phys. Rev. C* **93**, 064909 (2016). 1512.00692.

53. Andronic, A., Braun-Munzinger, P., Stachel, J. & Stöcker, H. Production of Light Nuclei, Hypernuclei and Their Antiparticles in Relativistic Nuclear Collisions. *Phys. Lett. B* **697**, 203–207 (2011).

54. Sato, H. & Yazaki, K. On the Coalescence Model for High Energy Nuclear Reactions. *Phys. Lett. B* **98**, 153–157 (1981).

55. Steinheimer, J. *et al.* Hypernuclei, Dibaryon and Antinuclei Production in High Energy Heavy Ion Collisions: Thermal Production vs. Coalescence. *Phys. Lett. B* **714**, 85–91 (2012).

56. Armstrong, T. A. *et al.* Mass Dependence of Light Nucleus Production in Ultrarelativistic Heavy Ion Collisions. *Phys. Rev. Lett.* **83**, 5431–5434 (1999). nucl-ex/9907002.

57. Farhi, E. *et al.* Strange Matter. *Phys. Rev. D* **30**, 2379 (1984).

58. Farhi, E. *et al.* Searching for Strange Matter by Heavy-ion Activation. *Phys. Rev. D* **32**, 2452 (1985).

59. Schaffner, J. *et al.* Strange Hadronic Matter. *Phys. Rev. Lett.* **71**, 1328 (1993).

60. Abelev, B. I. *et al.* Identified Baryon and Meson Distributions at Large Transverse Momenta from Au+Au Collisions at $\sqrt{s_{NN}} = 200$ GeV. *Phys. Rev. Lett.* **97**, 152301 (2006). nucl-ex/0606003.

61. Sun, K.-J., Ko, C. M. & Dönigus, B. Suppression of light nuclei production in collisions of small systems at the Large Hadron Collider. *Phys. Lett. B* **792**, 132–137 (2019). 1812.05175.

62. Zhang, S. *et al.* Searching for Onset of Deconfinement via Hypernuclei and Baryon-strangeness Correlations. *Phys. Lett. B* **684**, 224–227 (2010). 0908.3357.

Methods

Event Sample and Trigger Selection. This analysis used 606 million and 624 million $\sqrt{s_{NN}} = 200$ GeV Au+Au collision events obtained in years 2010 and 2011, 512 million $\sqrt{s_{NN}} = 193$ GeV U+U collision events from year 2012, and 4.7 billion $\sqrt{s_{NN}} = 200$ GeV Ru+Ru and Zr+Zr collision events from year 2018.

The majority of events were collected with minimum bias (MB) triggers. The MB triggers required a coincidence between either the vertex position detectors (VPD) or the zero degree calorimeters (ZDC). The VPD [1] is a pair of timing detectors mounted directly around the beampipe that cover approximately half of the phase space over the pseudorapidity region $4.2 < |\eta| < 5.2$. The ZDC [2] is a pair of hadronic calorimeters located at $|\eta| > 6.6$ that detect spectator neutrons emerging from the heavy ion collisions.

Often the MB triggers were highly prescaled to reserve a fraction of the data acquisition bandwidth for triggers on rare processes. Events that satisfied "central" or "non-photonic electron" triggers were included in the analysis to enhance the overall statistics. The central triggers combined multiplicity information from the time-of-flight system [3] with spectator neutron multiplicity information from the ZDCs to select collisions with small impact parameters. The non-photonic electron triggers required a large transverse energy deposition ($E_T > 2.6$, 3.5, or 4.2 GeV) in at least one $\Delta\eta \times \Delta\phi = 0.05 \times 0.05$ tower in the barrel electromagnetic calorimeter [4]. It has a high probability to trigger on events containing anti-nuclei, which may annihilate in the electromagnetic calorimeter. Events triggered by the "central" or "non-photonic electron" triggers were not used in

the yield ratios analysis to avoid potential biases.

The reconstructed collision point, called the primary vertex, is required to be within 2 cm from the beam line and within 40 cm along the beam line from the detector center.

Particle Identification and Topological Reconstruction. Information from the TPC and the TOF are combined for particle identification. The cylindrical TPC has full azimuthal coverage in the pseudorapidity range $-1 < \eta < 1$. In order to ensure good track quality, a minimum of 20 measured points in TPC are required for all tracks used in this analysis. A selected ^{3}He or $^3\overline{\text{He}}$ candidate should satisfy $|n_{\sigma^3\text{He}}| < 3$. If the track has matched TOF hit information, it should also satisfy the condition $1.0 < m^2/Z^2 < 3.0$ (GeV/c^2)^2. For ^{4}He and $^4\overline{\text{He}}$ selection, in addition to $|n_{\sigma^4\text{He}}| < 3$, it is also required that $2.8 < m^2/Z^2 < 4.1$ (GeV/c^2)^2 if a matching TOF hit is present or $|n_{\sigma^3\text{He}}| > 3.5$ if there is no TOF match, in order to minimize contamination from ^{3}He and $^3\overline{\text{He}}$, which have much higher production yields. In order to reject background ^{3}He and ^{4}He knocked out from the beam pipe and other materials, the distance of closest approach (DCA) between the ^{3}He or ^{4}He trajectory and the primary vertex is required to be within 1 cm. This DCA requirement is not applied to $^3\overline{\text{He}}$ and $^4\overline{\text{He}}$ since there are no knock-out antinuclei. The daughter $\pi^\pm$ from (anti)hypernucleus decay is identified by requiring $|n_{\sigma\pi^\pm}| < 3$. A m^2/Z^2 cut is also applied if the track is associated with a TOF hit.

(Anti-)hypernucleus candidates are reconstructed from the selected $\pi^\pm$ and (anti-)helium nucleus tracks by the Kalman-Filter (KF) Particle Finder package [5,6], which is based on the Kalman filter method. The decay topology of hypernuclei is characterized by several variables: χ^2_{topo} de-

scribing the likelihood that the path of the reconstructed mother particle goes through the primary vertex, χ^2_{NDF} describing the likelihood that the two daughter tracks come from a common decay vertex, $\chi^2_{primary}$ describing the likelihood that the decay daughter track comes from the primary vertex, the decay length (L), and L over its uncertainty (L/dL). Topological selection cuts are optimized for the best ${}^{3}_{\Lambda}\overline{\mathrm{H}}$ signal and listed in Tab. 1.

Table 1: Topological cuts for (anti)hypernucleus selection.

Particles	χ^2_{topo}	χ^2_{NDF}	π $\chi^2_{primary}$	He $\chi^2_{primary}$	L(cm)	L/dL	He DCA
${}^{3}_{\Lambda}\mathrm{H}$, ${}^{4}_{\Lambda}\mathrm{H}$	< 2	< 5	> 10	< 2000	> 3.5	> 3.4	$< 1cm$
${}^{3}_{\Lambda}\overline{\mathrm{H}}$, ${}^{4}_{\Lambda}\overline{\mathrm{H}}$	< 3	< 5	> 10	< 2000	> 3.5	> 3.4	$-$

Background Subtraction. The invariant mass distributions of the combinatorial backgrounds are reproduced with the rotation method. They are then scaled so that the their integrals in two side band regions ($2.941 \sim 2.987$ GeV/c^2 and $2.997 \sim 3.101$ GeV/c^2 for ${}^{3}_{\Lambda}\mathrm{H}$ and ${}^{3}_{\Lambda}\overline{\mathrm{H}}$, $3.859 \sim 3.919$ GeV/c^2 and $3.925 \sim 4.019$ GeV/c^2 for ${}^{4}_{\Lambda}\mathrm{H}$ and ${}^{4}_{\Lambda}\overline{\mathrm{H}}$) are equal to the integrals of the signal candidate invariant mass distributions in the same regions. After that, the signal counts are extracted by subtracting the integrals of the scaled combinatorial background distributions from the integrals of the signal candidate distributions in the signal invariant mass regions ($2.987 \sim 2.997$ GeV/c^2 for ${}^{3}_{\Lambda}\mathrm{H}$ and ${}^{3}_{\Lambda}\overline{\mathrm{H}}$, $3.919 \sim 3.925$ GeV/c^2 for ${}^{4}_{\Lambda}\mathrm{H}$ and ${}^{4}_{\Lambda}\overline{\mathrm{H}}$).

Significance Calculation. The statistical significance of an observation is introduced to quantify the probability of an excess in the signal invariant mass region originating purely from a statistical fluctuation of the background. For large statistics, the measured count follows a Gaussian distribution, with standard deviation σ equal to the square root of the count. If the expected background

level is N_{Bg} while the measured total count is $N_{Sig} + N_{Bg}$, then $\sigma = \sqrt{N_{Sig} + N_{Bg}}$, and the number of standard deviations from the background level due to the signal is $N_\sigma = N_{Sig}/\sigma = N_{Sig}/\sqrt{N_{Sig} + N_{Bg}}$. This method is used to evaluate the significance for ${}^{3}_{\Lambda}\mathrm{H}$ and ${}^{3}_{\bar{\Lambda}}\overline{\mathrm{H}}$.

For ${}^{4}_{\Lambda}\mathrm{H}$ and ${}^{4}_{\bar{\Lambda}}\overline{\mathrm{H}}$, however, the expected numbers of signal and background counts are very low. The measured counts follow a Poisson distribution instead of a Gaussian. The Poisson distribution will approach a Gaussian distribution only in the large statistics limit. To describe the confidence of the observation of ${}^{4}_{\Lambda}\mathrm{H}$ and ${}^{4}_{\bar{\Lambda}}\overline{\mathrm{H}}$ signals, an equivalent Gaussian significance $N_{\sigma\ eq}$ is defined, so that the probability of observing an excess larger than $N_{\sigma\ eq}$ standard deviations above the expected background level in a Gaussian distribution

$$p_{Gaussian} = \int_{N_{\sigma\ eq}}^{+\infty} \frac{1}{\sqrt{2\pi}} \exp\left(-\frac{x^2}{2}\right) dx, \tag{1}$$

is equal to the probability of observing no fewer than $N_{Sig} + N_{Bg}$ counts in the Poisson distribution with the expected background level of N_{Bg}

$$p_{Poisson} = \sum_{n=N_{Sig}+N_{Bg}}^{+\infty} \frac{N_{Bg}^n}{n!} \exp\left(-N_{Bg}\right). \tag{2}$$

This is illustrated in Fig. 1. The shaded area in panel (b) beyond $N_{\sigma\ eq}$ is equal to the shaded area in panel (a) beyond the measured $N_{Sig} + N_{Bg}$. For ${}^{4}_{\bar{\Lambda}}\overline{\mathrm{H}}$, the probability calculated with Eq. 2 is 1.0×10^{-6}, which gives an equivalent Gaussian significance $N_{\sigma\ eq}$ of 4.7 according to Eq. 1. Considering that a $N_{\sigma\ eq} = 5.4$ signal of ${}^{4}_{\Lambda}\mathrm{H}$ is also observed with almost the same reconstruction procedure and selection criteria, the discovery of ${}^{4}_{\bar{\Lambda}}\overline{\mathrm{H}}$ has been made.

Efficiency Corrections. A correction is applied for the detector acceptance and reconstruction efficiency in the lifetime and yield ratio measurements. The acceptance and efficiency are ob-

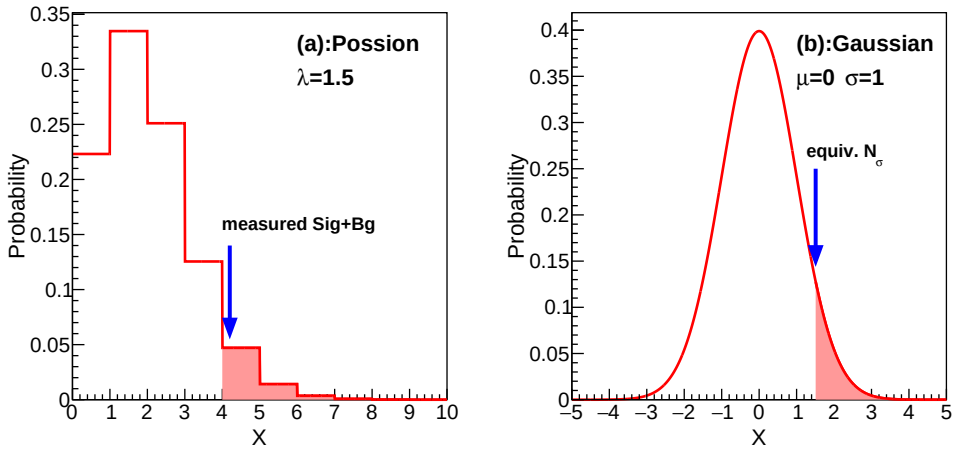

Figure 1: Illustration of calculation of equivalent Gaussian significance $N_{\sigma\ eq}$. The shaded regions of the Poisson distribution in panel (a) and the Gaussian distribution in panel (b) have the same area, indicating the same probability of excesses beyond the expected background level purely due to fluctuations.

tained with an embedding Monte Carlo (MC) technique. (Anti-)hypernuclei are simulated using a GEANT3 package, taking into account the geometry and materials of the STAR detectors [7]. The physical processes and the responses of the read-out electronics are simulated, and the final simulated data are embedded into real data events, which are sampled from different data-taking runs to have a good representation of the whole data set used in the analysis. The number of MC (anti-)hypernuclei embedded is 5% of the multiplicity of the real data events. Then the embedded events are processed through the same reconstruction procedures as real data. After that, the same track and topological requirements as for the real data are applied to the reconstructed MC (anti-)hypernuclei. The final reconstruction efficiency is calculated as the ratio of the number of reconstructed MC (anti-)hypernuclei to the number of input MC (anti-)hypernuclei. This efficiency

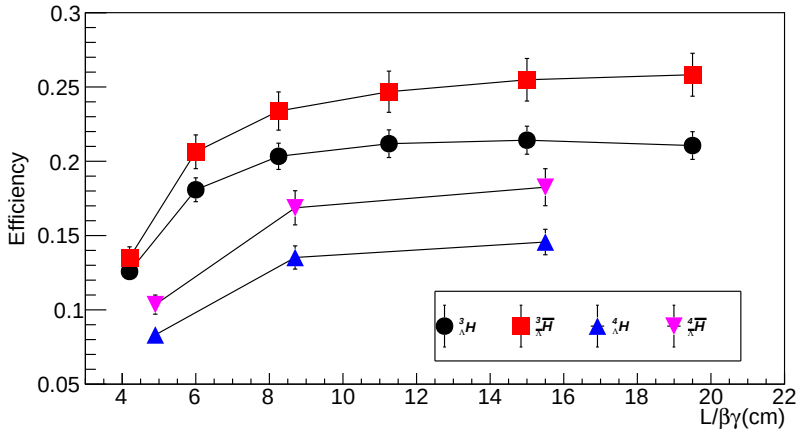

Figure 2: Reconstruction efficiency as a function of $L/(\beta\gamma)$ obtained from the embedding Monte Carlo technique. As shown in Tab. 1, hypernuclei have stricter topological cuts than anti-hypernuclei to suppress knock-out ^{3}He and ^{4}He, resulting in lower efficiency.

includes the detector acceptance, tracking efficiency and selection efficiency.

The (anti-)hypernucleus reconstruction efficiencies as a function of $L/(\beta\gamma)$ are shown in Fig. 2, which are used to correct the raw yields in different $L/(\beta\gamma)$ intervals before the exponential fits are conducted to extract the lifetimes.

(Anti)hypernuclei, Λ and $\bar{\Lambda}$ lifetime measurements. Figure 3 shows the invariant mass distributions of ${}^3_{\Lambda}\mathrm{H}$, ${}^3_{\bar{\Lambda}}\overline{\mathrm{H}}$, ${}^4_{\Lambda}\mathrm{H}$ and ${}^4_{\bar{\Lambda}}\overline{\mathrm{H}}$ candidates in different $L/(\beta\gamma)$ intervals, which are used to extract their lifetimes.

As an additional test of (anti)hypernucleus lifetime measurements, we have also measured the Λ and $\bar{\Lambda}$ lifetimes with the same method. 3.2 million Au+Au collision events at $\sqrt{s_{NN}} = 200$ GeV are used for these measurements. The topological cuts used to obtain the Λ signal are the

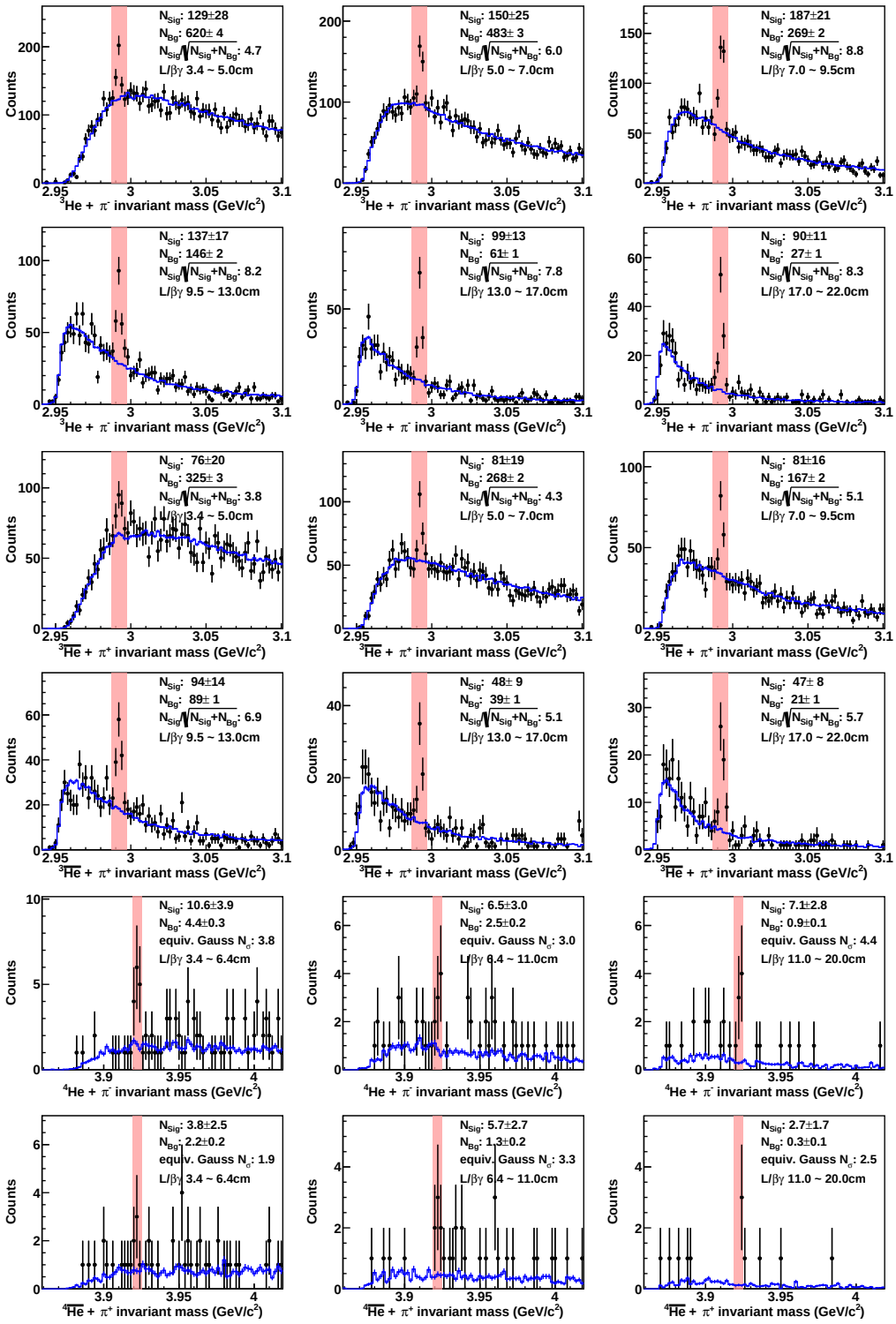

Figure 3: ${}^{3}_{\Lambda}\mathrm{H}$, ${}^{3}_{\Lambda}\overline{\mathrm{H}}$, ${}^{4}_{\Lambda}\mathrm{H}$ and ${}^{4}_{\Lambda}\overline{\mathrm{H}}$ candidate invariant mass distributions in different $L/\beta\gamma$ intervals.

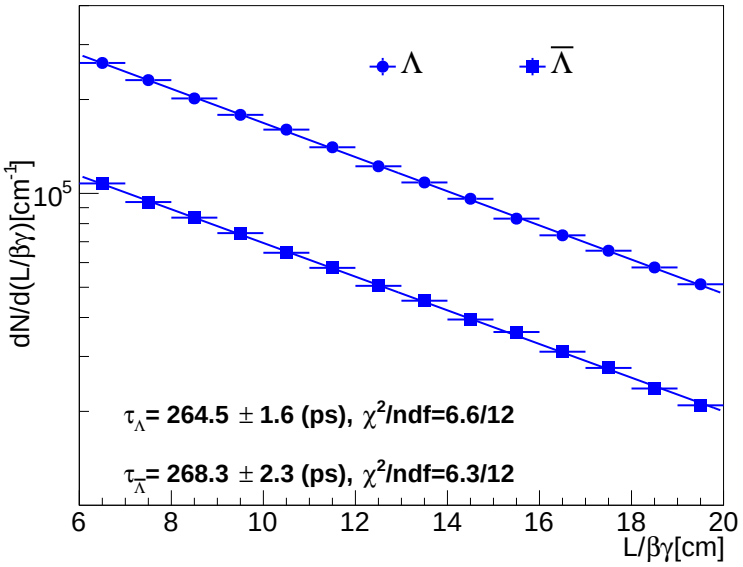

Figure 4: $dN/d(L/\beta\gamma)$ as a function of $L/\beta\gamma$ for Λ and $\bar{\Lambda}$, and exponential fits to obtain their lifetimes.

same as those used in the (anti)hypernucleus analysis, except that an additional $V_0DCA < 0.1$ cm topological cut is added. V_0DCA is the distance of closest approach between the reconstructed mother particle trajectory and the primary vertex. The V_0DCA cut suppresses contributions of Λ ($\bar{\Lambda}$) from Ξ ($\bar{\Xi}$) and Ω ($\bar{\Omega}$) decays, which make the measured lifetime longer. This is verified by the fact that the measured Λ and $\bar{\Lambda}$ lifetimes increase as the allowed V_0DCA range is enlarged. Figure 4 shows the Λ and $\bar{\Lambda}$ $L/\beta\gamma$ distributions, and the exponential fits to obtain their lifetimes. Our measured lifetimes for Λ (264.5$\pm$1.6 ps) and $\bar{\Lambda}$ (268.3$\pm$2.3 ps) are consistent considering uncertainties, as expected by the CPT symmetry. However, they are slightly longer than the value from the Particle Data Group 263$\pm$2 ps [8]. This is expected because the V_0DCA cut can not exclude all Λ from Ξ and Ω decays. No particle yet discovered decays to ${}^{3}_{\Lambda}$H or ${}^{4}_{\Lambda}$H, so we do not consider the decay feed-down effect for (anti)hypernuclei lifetime measurements in this analysis.

Yield Measurements. The yields of all the studied particles in this work are measured in the phase space of $|Rapidity| < 0.7$ and $0.7c < p_{\rm T}/m < 1.5c$ with only MB triggered events. Thus the (anti)hypernucleus signal counts are less than those in Fig. 3 in this paper. The signal and background counts that are used to extract (anti)hypernuclei yield ratios are listed in the Tab. 2.

Table 2: The signal and background counts in the measured phase space with MB triggered events.

Collision systems		${}^{3}_{\Lambda}\mathrm{H}$	${}^{3}_{\bar{\Lambda}}\overline{\mathrm{H}}$	${}^{4}_{\Lambda}\mathrm{H}$	${}^{4}_{\bar{\Lambda}}\overline{\mathrm{H}}$
Total	N_{Sig}	816 ± 53	472 ± 40	23.1 ± 5.7	12.1 ± 4.1
	N_{Bg}	1951 ± 6	1131 ± 5	8.9 ± 0.4	4.9 ± 0.3
Au+Au, U+U	N_{Sig}	378 ± 41	224 ± 35	-	-
	N_{Bg}	1263 ± 5	750 ± 4	-	-
Zr+Zr, Ru+Ru	N_{Sig}	441 ± 34	248 ± 25	-	-
	N_{Bg}	685 ± 3	381 ± 3	-	-

After $|n_{\sigma^3\mathrm{He}}| < 3$ and $1 < M^2/Q^2 < 3$ (GeV/c^2)^2 selections, the ^{3}He and $^3\overline{\mathrm{He}}$ candidates are counted with a 1/efficiency weight to get the yield in the measured phase space.

For ${}^{3}_{\Lambda}\mathrm{H}$ and ${}^{3}_{\bar{\Lambda}}\overline{\mathrm{H}}$ yield measurements, invariant mass distributions are obtained with a candidate-by-candidate 1/efficiency weight. Then the signal yield is extracted by subtracting the combinatorial background, obtained by the rotation method, from the candidate invariant mass distribution in the signal range.

For ^{4}He, $^4\overline{\mathrm{He}}$, ${}^{4}_{\Lambda}\mathrm{H}$ and ${}^{4}_{\bar{\Lambda}}\overline{\mathrm{H}}$, the statistics are too low to apply a candidate-by-candidate efficiency correction. We thus calculated the total raw yields in the whole selected $p_{\rm T}$ range and

corrected it by the average efficiency. The average efficiency is obtained based on knowledge of the $p_{\rm T}$ spectra of $A = 3$ (anti)(hyper)nuclei. Firstly, the $p_{\rm T}$ spectra for ^{3}He, $^3\overline{\rm He}$, $^3_\Lambda$H and $^3_{\overline{\Lambda}}\overline{\rm H}$ are obtained and fitted with Blast-Wave (BW) functions [9]

$$\frac{1}{2\pi p_T}\frac{d^2N}{dp_T dy} \propto \int_0^R r dr m_0 I_0\left(\frac{p_T \sinh\rho}{T}\right) K_1\left(\frac{m_T \cosh\rho}{T}\right), \tag{3}$$

as shown in Fig. 5. Here $\rho = \tanh^{-1}(\beta_s(r/R)^n)$ and $n = 1$. The fireball radius R is 10 fm. I_0 and K_1 are Bessel functions. m_0 is the particle mass, and $m_T = \sqrt{m_0^2 + p_T^2}$. β_s and T are free fitting parameters, representing the expansion velocity and temperature of the fireball. We then assume the BW functions for ^{4}He, $^4\overline{\rm He}$, $^4_\Lambda$H and $^4_{\overline{\Lambda}}\overline{\rm H}$ have the same β_s and T as for ^{3}He, $^3\overline{\rm He}$, $^3_\Lambda$H and $^3_{\overline{\Lambda}}\overline{\rm H}$, respectively, and the only difference in the BW functions are the particle masses. The efficiencies for ^{4}He, $^4\overline{\rm He}$, $^4_\Lambda$H and $^4_{\overline{\Lambda}}\overline{\rm H}$ in the whole measured p_T range are calculated as the average efficiency with the above BW function weights. The measured raw yields of ^{4}He, $^4\overline{\rm He}$, $^4_\Lambda$H and $^4_{\overline{\Lambda}}\overline{\rm H}$ are then corrected with the average efficiencies to obtain the physics yields.

The yields of ^{3}He, $^3\overline{\rm He}$, ^{4}He and $^4\overline{\rm He}$ are also corrected for the contributions from the weak decays of $^3_\Lambda$H, $^3_{\overline{\Lambda}}\overline{\rm H}$, $^4_\Lambda$H and $^4_{\overline{\Lambda}}\overline{\rm H}$, whose fractions out of the total measured (anti)helium nuclei yields are listed in Tab. 3.

Systematic Uncertainties. Four major sources of systematic uncertainties are evaluated for the (anti)hypernucleus lifetime measurements and the yield ratio measurements: A. Systematic uncertainties on track reconstruction efficiency, evaluated by varying the minimal number of measured points on the tracks; B. Systematic uncertainties on (anti)hypernucleus reconstruction efficiency due to topological selections, evaluated by varying the topological selection viarables; C. System-

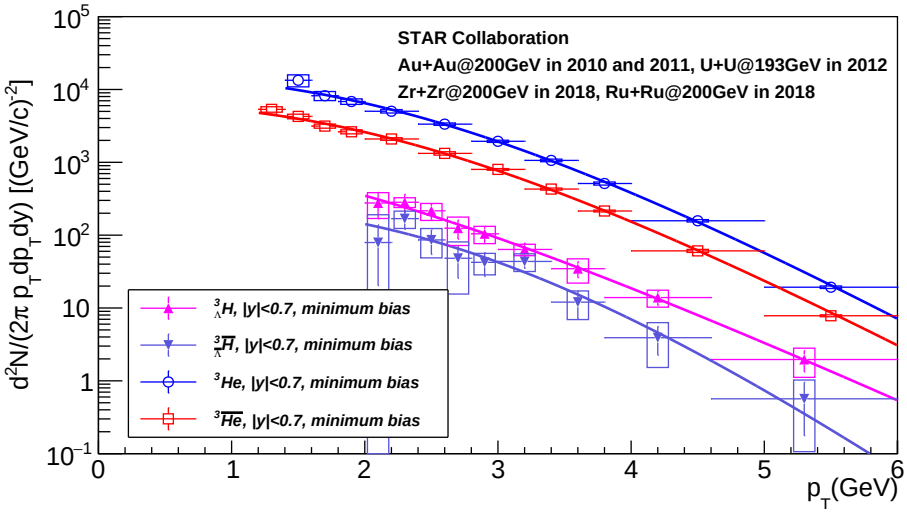

Figure 5: Efficiency corrected p_T spectra for ^{3}He, $^3\overline{\text{He}}$, $^3_\Lambda$H, and $^3_\Lambda\overline{\text{H}}$. The spectra are not normalized by the number of events. The lines represent the BW function fits.

Table 3: Fraction of (anti)helium nuclei from the weak decays of (anti)hypernuclei in different collision systems.

Collision systems	^{3}He	$^3\overline{\text{He}}$	^{4}He	$^4\overline{\text{He}}$
Total	4.4%	4.9%	29%	43%
Au+Au, U+U	5.5%	6.2%	-	-
Zr+Zr, Ru+Ru	3.6%	4.0%	-	-

atic uncertainties on (anti)hypernucleus signal yield extraction from the invariant mass spectra, evaluated by enlarging the invariant mass ranges for signal yield integration; and systematic uncertainties from the p_T spectra shape, evaluated by narrowing the p_T spectra fit ranges. D. Systematic uncertainties on the (anti)helium yields, evaluated by varying the minimal number of measured points for $\langle dE/dx \rangle$ calculation and the cut on the helium track DCA to primary vertex. The total systematic uncertainty is calculated as the quadratic sum of the four contributions above. The systematic uncertainty contributions from different sources for lifetime and yield ratio measurements are summarized in Tab. 4, Tab. 5 and Tab. 6.

Table 4: Systematic uncertainties on (anti)hypernucleus lifetimes.

Sources	$\tau(^{3}_{\Lambda}\mathrm{H})$	$\tau(^{3}_{\bar{\Lambda}}\overline{\mathrm{H}})$	$\tau(^{4}_{\Lambda}\mathrm{H})$	$\tau(^{4}_{\bar{\Lambda}}\overline{\mathrm{H}})$
Track reconstruction	2.8%	8.9%	15.5%	16.8%
Topological selection	4.5%	7.3%	11.9%	10.5%
Signal extraction & p_T shape	0.4%	0.5%	2.4%	3.8%
Total	5.4%	11.6%	19.7%	20.1%

Table 5: Systematic uncertainties on yield ratios in all measured collision systems.

Sources	$\frac{^{3}\overline{\mathrm{He}}}{^{3}\mathrm{He}}$	$\frac{^{4}\overline{\mathrm{He}}}{^{4}\mathrm{He}}$	$\frac{^{3}_{\bar{\Lambda}}\overline{\mathrm{H}}}{^{3}_{\Lambda}\mathrm{H}}$	$\frac{^{4}_{\bar{\Lambda}}\overline{\mathrm{H}}}{^{4}_{\Lambda}\mathrm{H}}$	$\frac{^{3}_{\Lambda}\mathrm{H}}{^{3}\mathrm{He}}$	$\frac{^{4}_{\Lambda}\mathrm{H}}{^{4}\mathrm{He}}$	$\frac{^{3}_{\bar{\Lambda}}\overline{\mathrm{H}}}{^{3}\overline{\mathrm{He}}}$	$\frac{^{4}_{\bar{\Lambda}}\overline{\mathrm{H}}}{^{4}\overline{\mathrm{He}}}$
Track reconstruction	0.6%	0.6%	12.6%	12.6%	5.8%	5.8%	10.8%	10.8%
Topological selection	0.5%	0.5%	10.1%	10.1%	3.8%	3.8%	13.6%	13.6%
Signal extraction & p_T shape	0.1%	22.8%	1.9%	46.3%	6.0%	20.4%	8.1%	50.8%
(Anti)helium yields	0.3%	0.3%	-	-	3.5%	3.5%	3.2%	3.2%
Total	0.9%	22.8%	16.2%	49.0%	9.8%	21.9%	19.5%	53.8%

Table 6: Systematic uncertainties on yield ratios in big and small collision systems.

	Au+Au, U+U		Zr+Zr, Ru+Ru	
Sources	$\frac{^3_\Lambda\mathrm{H}}{^3\mathrm{He}}$	$\frac{^3_\Lambda\overline{\mathrm{H}}}{^3\overline{\mathrm{He}}}$	$\frac{^3_\Lambda\mathrm{H}}{^3\mathrm{He}}$	$\frac{^3_\Lambda\overline{\mathrm{H}}}{^3\overline{\mathrm{He}}}$
Track reconstruction	8.1%	26.9%	3.6%	4.9%
Topological selection	7.0%	27.7%	3.7%	7.9%
Signal extraction & p_T shape	15.1%	18.2%	3.0%	0.6%
(Anti)helium yields	4.2%	3.5%	3.8%	1.9%
Total	19.0%	42.8%	7.1%	9.5%

Reference

1. Llope, W. *et al.* The TOFp/pVPD Time-of-flight System for STAR. *Nuclear Instruments and Methods A* **522**, 252–273 (2004).

2. Adler, C. *et al.* The RHIC Zero Degree Calorimeters. *Nuclear Instruments and Methods A* **470**, 488–499 (2001).

3. Llope, W. J. and STAR collaboration et al. Multigap RPCs in the STAR Experiment at RHIC. *Nuclear Instruments and Methods A* **661**, S110–S113 (2012).

4. Beddo, M. *et al.* The STAR Barrel Electromagnetic Calorimeter. *Nuclear Instruments and Methods A* **499**, 725–739 (2003). The Relativistic Heavy Ion Collider Project: RHIC and its Detectors.

5. Kisel, I., Kulakov, I. & Zyzak, M. Standalone First Level Event Selection Package for the CBM

Experiment. In *Proceedings, 18th Real-Time Conference (RT2012) : Berkley, USA, June 11-15, 2012* (2012).

6. Zyzak, M. *Online Selection of Short-lived Particles on Many-core Computer Architectures in the CBM Experiment at FAIR*. Ph.D. thesis, Johann Wolfgang Goethe-Universität (2016).

7. Fine, V. & Nevski, P. OO Model of STAR Detector for Simulation, Visualisation and Reconstruction. In *11th International Conference on Computing in High-Energy and Nuclear Physics*, 143–146 (2000).

8. Group, P. D. *et al.* Review of Particle Physics. *Progress of Theoretical and Experimental Physics* **2022**, 083C01 (2022).

9. Schnedermann, E., Sollfrank, J. & Heinz, U. W. Thermal Phenomenology of Hadrons from 200-A/GeV S+S Collisions. *Phys. Rev. C* **48**, 2462–2475 (1993). `nucl-th/9307020`.